

Measurement of Michel Parameters ($\bar{\eta}$, $\xi\kappa$) in the radiative leptonic decay $\tau \rightarrow l\nu\bar{\nu}\gamma$ at Belle

A. Abdesselam,⁹² I. Adachi,^{20,16} K. Adamczyk,⁶⁶ H. Aihara,¹⁰⁰ S. Al Said,^{92,42}
K. Arinstein,^{5,70} Y. Arita,⁵⁹ D. M. Asner,⁷³ T. Aso,¹⁰⁵ H. Atmacan,⁵⁵ V. Aulchenko,^{5,70}
T. Aushev,⁵⁸ R. Ayad,⁹² T. Aziz,⁹³ V. Babu,⁹³ I. Badhrees,^{92,41} S. Bahinipati,²⁶
A. M. Bakich,⁹¹ A. Bala,⁷⁴ Y. Ban,⁷⁵ V. Bansal,⁷³ E. Barberio,⁵⁴ M. Barrett,¹⁹ W. Bartel,¹⁰
A. Bay,⁴⁷ P. Behera,²⁸ M. Belhorn,⁹ K. Belous,³² M. Berger,⁸⁹ D. Besson,⁵⁷ V. Bhardwaj,²⁵
B. Bhuyan,²⁷ J. Biswal,³⁶ T. Bloomfield,⁵⁴ S. Blyth,⁶⁴ A. Bobrov,^{5,70} A. Bondar,^{5,70}
G. Bonvicini,¹⁰⁸ C. Bookwalter,⁷³ C. Boulahouache,⁹² A. Bozek,⁶⁶ M. Bračko,^{52,36}
F. Breibeck,³¹ J. Brodzicka,⁶⁶ T. E. Browder,¹⁹ E. Waheed,⁵⁴ D. Červenkov,⁶ M.-C. Chang,¹²
P. Chang,⁶⁵ Y. Chao,⁶⁵ V. Chekelian,⁵³ A. Chen,⁶³ K.-F. Chen,⁶⁵ P. Chen,⁶⁵ B. G. Cheon,¹⁸
K. Chilikin,^{48,57} R. Chistov,^{48,57} K. Cho,⁴³ V. Chobanova,⁵³ S.-K. Choi,¹⁷ Y. Choi,⁹⁰
D. Cinabro,¹⁰⁸ J. Crnkovic,²⁴ J. Dalseno,^{53,94} M. Danilov,^{57,48} N. Dash,²⁶ S. Di Carlo,¹⁰⁸
J. Dingfelder,⁴ Z. Doležal,⁶ D. Dossett,⁵⁴ Z. Drásal,⁶ A. Drutskoy,^{48,57} S. Dubey,¹⁹
D. Dutta,⁹³ K. Dutta,²⁷ S. Eidelman,^{5,70} D. Epifanov,^{5,70} H. Farhat,¹⁰⁸ J. E. Fast,⁷³
M. Feindt,³⁸ T. Ferber,¹⁰ A. Frey,¹⁵ O. Frost,¹⁰ B. G. Fulsom,⁷³ V. Gaur,⁹³ N. Gabyshev,^{5,70}
S. Ganguly,¹⁰⁸ A. Garmash,^{5,70} D. Getzkow,¹³ R. Gillard,¹⁰⁸ F. Giordano,²⁴ R. Glattauer,³¹
Y. M. Goh,¹⁸ P. Goldenzweig,³⁸ B. Golob,^{49,36} D. Greenwald,⁹⁵ M. Grosse Perdekamp,^{24,81}
J. Grygier,³⁸ O. Grzymkowska,⁶⁶ Y. Guan,^{29,20} H. Guo,⁸³ J. Haba,^{20,16} P. Hamer,¹⁵
Y. L. Han,³⁰ K. Hara,²⁰ T. Hara,^{20,16} Y. Hasegawa,⁸⁵ J. Hasenbusch,⁴ K. Hayasaka,⁶⁸
H. Hayashii,⁶² X. H. He,⁷⁵ M. Heck,³⁸ M. T. Hedges,¹⁹ D. Heffernan,⁷² M. Heider,³⁸
A. Heller,³⁸ T. Higuchi,³⁹ S. Himori,⁹⁸ S. Hirose,⁵⁹ T. Horiguchi,⁹⁸ Y. Hoshi,⁹⁷ K. Hoshina,¹⁰³
W.-S. Hou,⁶⁵ Y. B. Hsiung,⁶⁵ C.-L. Hsu,⁵⁴ M. Huschle,³⁸ H. J. Hyun,⁴⁶ Y. Igarashi,²⁰
T. Iijima,^{60,59} M. Imamura,⁵⁹ K. Inami,⁵⁹ G. Inguglia,¹⁰ A. Ishikawa,⁹⁸ K. Itagaki,⁹⁸
R. Itoh,^{20,16} M. Iwabuchi,¹¹⁰ M. Iwasaki,¹⁰⁰ Y. Iwasaki,²⁰ S. Iwata,¹⁰² W. W. Jacobs,²⁹
I. Jaegle,¹¹ H. B. Jeon,⁴⁶ Y. Jin,¹⁰⁰ D. Joffe,⁴⁰ M. Jones,¹⁹ K. K. Joo,⁸ T. Julius,⁵⁴
H. Kakuno,¹⁰² A. B. Kaliyar,²⁸ J. H. Kang,¹¹⁰ K. H. Kang,⁴⁶ P. Kapusta,⁶⁶ S. U. Kataoka,⁶¹
E. Kato,⁹⁸ Y. Kato,⁵⁹ P. Katrenko,^{58,48} H. Kawai,⁷ T. Kawasaki,⁶⁸ T. Keck,³⁸ H. Kichimi,²⁰
C. Kiesling,⁵³ B. H. Kim,⁸⁴ D. Y. Kim,⁸⁷ H. J. Kim,⁴⁶ H.-J. Kim,¹¹⁰ J. B. Kim,⁴⁴
J. H. Kim,⁴³ K. T. Kim,⁴⁴ M. J. Kim,⁴⁶ S. H. Kim,¹⁸ S. K. Kim,⁸⁴ Y. J. Kim,⁴³
K. Kinoshita,⁹ C. Kleinwort,¹⁰ J. Klucar,³⁶ B. R. Ko,⁴⁴ N. Kobayashi,¹⁰¹ S. Koblitz,⁵³
P. Kodyš,⁶ Y. Koga,⁵⁹ S. Korpar,^{52,36} D. Kotchetkov,¹⁹ R. T. Kouzes,⁷³ P. Križan,^{49,36}
P. Krokovny,^{5,70} B. Kronenbitter,³⁸ T. Kuhr,⁵⁰ R. Kulasiri,⁴⁰ R. Kumar,⁷⁷ T. Kumita,¹⁰²
E. Kurihara,⁷ Y. Kuroki,⁷² A. Kuzmin,^{5,70} P. Kvasnička,⁶ Y.-J. Kwon,¹¹⁰ Y.-T. Lai,⁶⁵
J. S. Lange,¹³ D. H. Lee,⁴⁴ I. S. Lee,¹⁸ S.-H. Lee,⁴⁴ M. Leitgab,^{24,81} R. Leitner,⁶ D. Levit,⁹⁵
P. Lewis,¹⁹ C. H. Li,⁵⁴ H. Li,²⁹ J. Li,⁸⁴ L. Li,⁸³ X. Li,⁸⁴ Y. Li,¹⁰⁷ L. Li Gioi,⁵³ J. Libby,²⁸
A. Limosani,⁵⁴ C. Liu,⁸³ Y. Liu,⁹ Z. Q. Liu,³⁰ D. Liventsev,^{107,20} A. Loos,⁸⁸ R. Louvot,⁴⁷
M. Lubej,³⁶ P. Lukin,^{5,70} T. Luo,⁷⁶ J. MacNaughton,²⁰ M. Masuda,⁹⁹ T. Matsuda,⁵⁶
D. Matvienko,^{5,70} A. Matyja,⁶⁶ S. McOnie,⁹¹ Y. Mikami,⁹⁸ K. Miyabayashi,⁶² Y. Miyachi,¹⁰⁹
H. Miyake,^{20,16} H. Miyata,⁶⁸ Y. Miyazaki,⁵⁹ R. Mizuk,^{48,57,58} G. B. Mohanty,⁹³
S. Mohanty,^{93,106} D. Mohapatra,⁷³ A. Moll,^{53,94} H. K. Moon,⁴⁴ T. Mori,⁵⁹ T. Morii,³⁹
H.-G. Moser,⁵³ T. Müller,³⁸ N. Muramatsu,⁷⁸ R. Mussa,³⁴ T. Nagamine,⁹⁸ Y. Nagasaka,²²
Y. Nakahama,¹⁰⁰ I. Nakamura,^{20,16} K. R. Nakamura,²⁰ E. Nakano,⁷¹ H. Nakano,⁹⁸
T. Nakano,⁷⁹ M. Nakao,^{20,16} H. Nakayama,^{20,16} H. Nakazawa,⁶³ T. Nanut,³⁶ K. J. Nath,²⁷
Z. Natkaniec,⁶⁶ M. Nayak,^{108,20} E. Nedelkovska,⁵³ K. Negishi,⁹⁸ K. Neichi,⁹⁷ C. Ng,¹⁰⁰

C. Niebuhr,¹⁰ M. Niiyama,⁴⁵ N. K. Nisar,^{93,1} S. Nishida,^{20,16} K. Nishimura,¹⁹ O. Nitoh,¹⁰³
T. Nozaki,²⁰ A. Ogawa,⁸¹ S. Ogawa,⁹⁶ T. Ohshima,⁵⁹ S. Okuno,³⁷ S. L. Olsen,⁸⁴ Y. Ono,⁹⁸
Y. Onuki,¹⁰⁰ W. Ostrowicz,⁶⁶ C. Oswald,⁴ H. Ozaki,^{20,16} P. Pakhlov,^{48,57} G. Pakhlova,^{48,58}
B. Pal,⁹ H. Palka,⁶⁶ E. Panzenböck,^{15,62} C.-S. Park,¹¹⁰ C. W. Park,⁹⁰ H. Park,⁴⁶ K. S. Park,⁹⁰
S. Paul,⁹⁵ L. S. Peak,⁹¹ T. K. Pedlar,⁵¹ T. Peng,⁸³ L. Pesántez,⁴ R. Pestotnik,³⁶
M. Peters,¹⁹ M. Petrič,³⁶ L. E. Piilonen,¹⁰⁷ A. Poluektov,^{5,70} K. Prasanth,²⁸ M. Prim,³⁸
K. Prothmann,^{53,94} C. Pulvermacher,²⁰ M. V. Purohit,⁸⁸ J. Rauch,⁹⁵ B. Reisert,⁵³ E. Ríbežl,³⁶
M. Ritter,⁵⁰ J. Rorie,¹⁹ A. Rostomyan,¹⁰ M. Rozanska,⁶⁶ S. Rummel,⁵⁰ S. Ryu,⁸⁴ H. Sahoo,¹⁹
T. Saito,⁹⁸ K. Sakai,²⁰ Y. Sakai,^{20,16} S. Sandilya,⁹ D. Santel,⁹ L. Santelj,²⁰ T. Sanuki,⁹⁸
J. Sasaki,¹⁰⁰ N. Sasao,⁴⁵ Y. Sato,⁵⁹ V. Savinov,⁷⁶ T. Schlüter,⁵⁰ O. Schneider,⁴⁷ G. Schnell,^{2,23}
P. Schönmeier,⁹⁸ M. Schram,⁷³ C. Schwanda,³¹ A. J. Schwartz,⁹ B. Schwenker,¹⁵ R. Seidl,⁸¹
Y. Seino,⁶⁸ D. Semmler,¹³ K. Senyo,¹⁰⁹ O. Seon,⁵⁹ I. S. Seong,¹⁹ M. E. Sevier,⁵⁴ L. Shang,³⁰
M. Shapkin,³² V. Shebalin,^{5,70} C. P. Shen,³ T.-A. Shibata,¹⁰¹ H. Shibuya,⁹⁶ N. Shimizu,¹⁰⁰
S. Shinomiya,⁷² J.-G. Shiu,⁶⁵ B. Shwartz,^{5,70} A. Sibidanov,⁹¹ F. Simon,^{53,94} J. B. Singh,⁷⁴
R. Sinha,³³ P. Smerkol,³⁶ Y.-S. Sohn,¹¹⁰ A. Sokolov,³² Y. Soloviev,¹⁰ E. Solovieva,^{48,58}
S. Stanič,⁶⁹ M. Starič,³⁶ M. Steder,¹⁰ J. F. Strube,⁷³ J. Stypula,⁶⁶ S. Sugihara,¹⁰⁰
A. Sugiyama,⁸² M. Sumihama,¹⁴ K. Sumisawa,^{20,16} T. Sumiyoshi,¹⁰² K. Suzuki,⁵⁹ K. Suzuki,⁸⁹
S. Suzuki,⁸² S. Y. Suzuki,²⁰ Z. Suzuki,⁹⁸ H. Takeichi,⁵⁹ M. Takizawa,^{86,21,80} U. Tamponi,^{34,104}
M. Tanaka,^{20,16} S. Tanaka,^{20,16} K. Tanida,³⁵ N. Taniguchi,²⁰ G. N. Taylor,⁵⁴ F. Tenchini,⁵⁴
Y. Teramoto,⁷¹ I. Tikhomirov,⁵⁷ K. Trabelsi,^{20,16} V. Trusov,³⁸ T. Tsuboyama,^{20,16}
M. Uchida,¹⁰¹ T. Uchida,²⁰ S. Uehara,^{20,16} K. Ueno,⁶⁵ T. Uglov,^{48,58} Y. Unno,¹⁸
S. Uno,^{20,16} S. Uozumi,⁴⁶ P. Urquijo,⁵⁴ Y. Ushiroda,^{20,16} Y. Usov,^{5,70} S. E. Vahsen,¹⁹
C. Van Hulse,² P. Vanhoefer,⁵³ G. Varner,¹⁹ K. E. Varvell,⁹¹ K. Vervink,⁴⁷ A. Vinokurova,^{5,70}
V. Vorobyev,^{5,70} A. Vossen,²⁹ M. N. Wagner,¹³ E. Waheed,⁵⁴ C. H. Wang,⁶⁴ J. Wang,⁷⁵
M.-Z. Wang,⁶⁵ P. Wang,³⁰ X. L. Wang,^{73,20} M. Watanabe,⁶⁸ Y. Watanabe,³⁷ R. Wedd,⁵⁴
S. Wehle,¹⁰ E. White,⁹ E. Widmann,⁸⁹ J. Wiechczynski,⁶⁶ K. M. Williams,¹⁰⁷ E. Won,⁴⁴
B. D. Yabsley,⁹¹ S. Yamada,²⁰ H. Yamamoto,⁹⁸ J. Yamaoka,⁷³ Y. Yamashita,⁶⁷
M. Yamauchi,^{20,16} S. Yashchenko,¹⁰ H. Ye,¹⁰ J. Yelton,¹¹ Y. Yook,¹¹⁰ C. Z. Yuan,³⁰
Y. Yusa,⁶⁸ C. C. Zhang,³⁰ L. M. Zhang,⁸³ Z. P. Zhang,⁸³ L. Zhao,⁸³ V. Zhilich,^{5,70}
V. Zhukova,⁵⁷ V. Zhulanov,^{5,70} M. Ziegler,³⁸ T. Zivko,³⁶ A. Zupanc,^{49,36} and N. Zwahlen⁴⁷

(The Belle Collaboration)

¹*Aligarh Muslim University, Aligarh 202002*

²*University of the Basque Country UPV/EHU, 48080 Bilbao*

³*Beihang University, Beijing 100191*

⁴*University of Bonn, 53115 Bonn*

⁵*Budker Institute of Nuclear Physics SB RAS, Novosibirsk 630090*

⁶*Faculty of Mathematics and Physics, Charles University, 121 16 Prague*

⁷*Chiba University, Chiba 263-8522*

⁸*Chonnam National University, Kwangju 660-701*

⁹*University of Cincinnati, Cincinnati, Ohio 45221*

¹⁰*Deutsches Elektronen-Synchrotron, 22607 Hamburg*

¹¹*University of Florida, Gainesville, Florida 32611*

¹²*Department of Physics, Fu Jen Catholic University, Taipei 24205*

¹³*Justus-Liebig-Universität Gießen, 35392 Gießen*

¹⁴*Gifu University, Gifu 501-1193*

¹⁵*II. Physikalisches Institut, Georg-August-Universität Göttingen, 37073 Göttingen*

¹⁶*SOKENDAI (The Graduate University for Advanced Studies), Hayama 240-0193*

¹⁷*Gyeongsang National University, Chinju 660-701*

- ¹⁸*Hanyang University, Seoul 133-791*
- ¹⁹*University of Hawaii, Honolulu, Hawaii 96822*
- ²⁰*High Energy Accelerator Research Organization (KEK), Tsukuba 305-0801*
- ²¹*J-PARC Branch, KEK Theory Center,
High Energy Accelerator Research Organization (KEK), Tsukuba 305-0801*
- ²²*Hiroshima Institute of Technology, Hiroshima 731-5193*
- ²³*IKERBASQUE, Basque Foundation for Science, 48013 Bilbao*
- ²⁴*University of Illinois at Urbana-Champaign, Urbana, Illinois 61801*
- ²⁵*Indian Institute of Science Education and Research Mohali, SAS Nagar, 140306*
- ²⁶*Indian Institute of Technology Bhubaneswar, Satya Nagar 751007*
- ²⁷*Indian Institute of Technology Guwahati, Assam 781039*
- ²⁸*Indian Institute of Technology Madras, Chennai 600036*
- ²⁹*Indiana University, Bloomington, Indiana 47408*
- ³⁰*Institute of High Energy Physics, Chinese Academy of Sciences, Beijing 100049*
- ³¹*Institute of High Energy Physics, Vienna 1050*
- ³²*Institute for High Energy Physics, Protvino 142281*
- ³³*Institute of Mathematical Sciences, Chennai 600113*
- ³⁴*INFN - Sezione di Torino, 10125 Torino*
- ³⁵*Advanced Science Research Center,
Japan Atomic Energy Agency, Naka 319-1195*
- ³⁶*J. Stefan Institute, 1000 Ljubljana*
- ³⁷*Kanagawa University, Yokohama 221-8686*
- ³⁸*Institut für Experimentelle Kernphysik,
Karlsruher Institut für Technologie, 76131 Karlsruhe*
- ³⁹*Kavli Institute for the Physics and Mathematics of the Universe (WPI),
University of Tokyo, Kashiwa 277-8583*
- ⁴⁰*Kennesaw State University, Kennesaw, Georgia 30144*
- ⁴¹*King Abdulaziz City for Science and Technology, Riyadh 11442*
- ⁴²*Department of Physics, Faculty of Science,
King Abdulaziz University, Jeddah 21589*
- ⁴³*Korea Institute of Science and Technology Information, Daejeon 305-806*
- ⁴⁴*Korea University, Seoul 136-713*
- ⁴⁵*Kyoto University, Kyoto 606-8502*
- ⁴⁶*Kyungpook National University, Daegu 702-701*
- ⁴⁷*École Polytechnique Fédérale de Lausanne (EPFL), Lausanne 1015*
- ⁴⁸*P.N. Lebedev Physical Institute of the Russian Academy of Sciences, Moscow 119991*
- ⁴⁹*Faculty of Mathematics and Physics,
University of Ljubljana, 1000 Ljubljana*
- ⁵⁰*Ludwig Maximilians University, 80539 Munich*
- ⁵¹*Luther College, Decorah, Iowa 52101*
- ⁵²*University of Maribor, 2000 Maribor*
- ⁵³*Max-Planck-Institut für Physik, 80805 München*
- ⁵⁴*School of Physics, University of Melbourne, Victoria 3010*
- ⁵⁵*Middle East Technical University, 06531 Ankara*
- ⁵⁶*University of Miyazaki, Miyazaki 889-2192*
- ⁵⁷*Moscow Physical Engineering Institute, Moscow 115409*
- ⁵⁸*Moscow Institute of Physics and Technology, Moscow Region 141700*
- ⁵⁹*Graduate School of Science, Nagoya University, Nagoya 464-8602*
- ⁶⁰*Kobayashi-Maskawa Institute, Nagoya University, Nagoya 464-8602*
- ⁶¹*Nara University of Education, Nara 630-8528*
- ⁶²*Nara Women's University, Nara 630-8506*

- ⁶³National Central University, Chung-li 32054
⁶⁴National United University, Miao Li 36003
⁶⁵Department of Physics, National Taiwan University, Taipei 10617
⁶⁶H. Niewodniczanski Institute of Nuclear Physics, Krakow 31-342
⁶⁷Nippon Dental University, Niigata 951-8580
⁶⁸Niigata University, Niigata 950-2181
⁶⁹University of Nova Gorica, 5000 Nova Gorica
⁷⁰Novosibirsk State University, Novosibirsk 630090
⁷¹Osaka City University, Osaka 558-8585
⁷²Osaka University, Osaka 565-0871
⁷³Pacific Northwest National Laboratory, Richland, Washington 99352
⁷⁴Panjab University, Chandigarh 160014
⁷⁵Peking University, Beijing 100871
⁷⁶University of Pittsburgh, Pittsburgh, Pennsylvania 15260
⁷⁷Punjab Agricultural University, Ludhiana 141004
⁷⁸Research Center for Electron Photon Science,
Tohoku University, Sendai 980-8578
⁷⁹Research Center for Nuclear Physics, Osaka University, Osaka 567-0047
⁸⁰Theoretical Research Division, Nishina Center, RIKEN, Saitama 351-0198
⁸¹RIKEN BNL Research Center, Upton, New York 11973
⁸²Saga University, Saga 840-8502
⁸³University of Science and Technology of China, Hefei 230026
⁸⁴Seoul National University, Seoul 151-742
⁸⁵Shinshu University, Nagano 390-8621
⁸⁶Showa Pharmaceutical University, Tokyo 194-8543
⁸⁷Soongsil University, Seoul 156-743
⁸⁸University of South Carolina, Columbia, South Carolina 29208
⁸⁹Stefan Meyer Institute for Subatomic Physics, Vienna 1090
⁹⁰Sungkyunkwan University, Suwon 440-746
⁹¹School of Physics, University of Sydney, New South Wales 2006
⁹²Department of Physics, Faculty of Science, University of Tabuk, Tabuk 71451
⁹³Tata Institute of Fundamental Research, Mumbai 400005
⁹⁴Excellence Cluster Universe, Technische Universität München, 85748 Garching
⁹⁵Department of Physics, Technische Universität München, 85748 Garching
⁹⁶Toho University, Funabashi 274-8510
⁹⁷Tohoku Gakuin University, Tagajo 985-8537
⁹⁸Department of Physics, Tohoku University, Sendai 980-8578
⁹⁹Earthquake Research Institute, University of Tokyo, Tokyo 113-0032
¹⁰⁰Department of Physics, University of Tokyo, Tokyo 113-0033
¹⁰¹Tokyo Institute of Technology, Tokyo 152-8550
¹⁰²Tokyo Metropolitan University, Tokyo 192-0397
¹⁰³Tokyo University of Agriculture and Technology, Tokyo 184-8588
¹⁰⁴University of Torino, 10124 Torino
¹⁰⁵Toyama National College of Maritime Technology, Toyama 933-0293
¹⁰⁶Utkal University, Bhubaneswar 751004
¹⁰⁷Virginia Polytechnic Institute and State University, Blacksburg, Virginia 24061
¹⁰⁸Wayne State University, Detroit, Michigan 48202
¹⁰⁹Yamagata University, Yamagata 990-8560
¹¹⁰Yonsei University, Seoul 120-749

Abstract

We present the first measurement of the Michel parameters $\bar{\eta}$ and $\xi\kappa$ in the radiative leptonic decay of the τ lepton using 703 fb^{-1} of data collected with the Belle detector at the KEKB e^+e^- collider. The Michel parameters are measured by an unbinned maximum likelihood fit to the kinematic information of $e^+e^- \rightarrow \tau^+\tau^- \rightarrow (\pi^+\pi^0\bar{\nu})(l^-\nu\bar{\nu}\gamma)$ ($l = e$ or μ). The preliminary values of the measured Michel parameters are $\bar{\eta} = -2.0 \pm 1.5 \pm 0.8$ and $\xi\kappa = 0.6 \pm 0.4 \pm 0.2$, where the first error is statistical and the second is systematic.

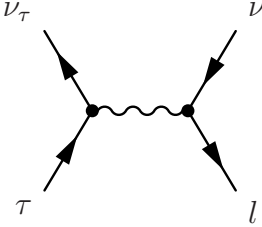
PACS numbers: 12.60Cn, 13.35Dx, 13.66.De, 13.66.Jn, 14.60.Fg

INTRODUCTION

In the Standard Model (SM), there are three flavors of charged leptons: e, μ and τ . The SM has proven to be the most powerful theory in describing the physics of leptons; nevertheless, precision tests of the SM may reveal the presence of New Physics (NP). In particular, measurement of the Michel parameters in τ decay is a powerful probe for NP.

The most general Lorentz-invariant derivative-free matrix element of leptonic τ decay $\tau^- \rightarrow l^- \nu \bar{\nu} \gamma$ [*] is represented as [1]

$\mathcal{M} =$



(1)

$$= \frac{4G_F}{\sqrt{2}} \sum_{\substack{N=S,V,T \\ i,j=L,R}} g_{ij}^N [\bar{u}_i(l)\Gamma^N v_n(\nu_l)] [\bar{u}_m(\nu_\tau)\Gamma_N u_j(\tau)],$$

where G_F is the Fermi constant, i and j are the chirality indices for the charged leptons, n and m are the chirality indices of the neutrinos, l is e or μ , $\Gamma^S = 1$, $\Gamma^V = \gamma^\mu$ and $\Gamma^T = i(\gamma^\mu\gamma^\nu - \gamma^\nu\gamma^\mu)/2\sqrt{2}$ are, respectively, the scalar, vector and tensor Lorentz structures in terms of the Dirac matrices γ^μ , u_i and v_i are the four-component spinors of a particle and an antiparticle, respectively and g_{ij}^N are the corresponding dimensionless couplings. In the SM, τ^- decays into l^- via the W^- vector boson with a right-handed antineutrino, *i.e.*, the only non-zero coupling is $g_{LL}^V = 1$. Experimentally, only the squared matrix element is observable and so bilinear combinations of the g_{ij}^N are accessible. Of all such combinations, four Michel parameters, η, ρ, δ and ξ , can be measured by the leptonic decay of the τ when the final state neutrinos are not observed [2]:

$$\rho = \frac{3}{4} - \frac{3}{4} \left(|g_{LR}^V|^2 + |g_{RL}^V|^2 + 2|g_{LR}^T|^2 + 2|g_{RL}^T|^2 + \Re(g_{LR}^S g_{LR}^{T*} + g_{RL}^S g_{RL}^{T*}) \right), \quad (2)$$

$$\eta = \frac{1}{2} \Re(6g_{RL}^V g_{LR}^{T*} + 6g_{LR}^V g_{RL}^{T*} + g_{RR}^S g_{LL}^{V*} + g_{RL}^S g_{LR}^{V*} + g_{LR}^S g_{RL}^{V*} + g_{LL}^S g_{RR}^{V*}), \quad (3)$$

$$\xi = 4\Re(g_{LR}^S g_{LR}^{T*} - g_{RL}^S g_{RL}^{T*}) + |g_{LL}^V|^2 + 3|g_{LR}^V|^2 - 3|g_{RL}^V|^2 - |g_{RR}^V|^2 + 5|g_{LR}^T|^2 - 5|g_{RL}^T|^2 + \frac{1}{4} \left(|g_{LL}^S|^2 - |g_{LR}^S|^2 + |g_{RL}^S|^2 - |g_{RR}^S|^2 \right), \quad (4)$$

$$\xi\delta = \frac{3}{16} \left(|g_{LL}^S|^2 - |g_{LR}^S|^2 + |g_{RL}^S|^2 - |g_{RR}^S|^2 \right) - \frac{3}{4} \left(|g_{LR}^T|^2 - |g_{RL}^T|^2 - |g_{LL}^V|^2 + |g_{RR}^V|^2 - \Re(g_{LR}^S g_{LR}^{T*} + g_{RL}^S g_{RL}^{T*}) \right). \quad (5)$$

The Feynman diagrams describing the radiative leptonic decay of the τ are presented in Fig. 1. As shown in Refs. [3, 4], the presence of a radiative photon in the final state (*radiative leptonic decay* or *inner bremsstrahlung*) exposes three more Michel parameters, $\bar{\eta}, \eta''$ and $\xi\kappa$:

$$\bar{\eta} = |g_{RL}^V|^2 + |g_{LR}^V|^2 + \frac{1}{8} \left(|g_{RL}^S + 2g_{RL}^T|^2 + |g_{LR}^S + 2g_{LR}^T|^2 \right) + 2 \left(|g_{RL}^T|^2 + |g_{LR}^T|^2 \right), \quad (6)$$

[*] Unless otherwise stated, use of charge-conjugate modes is implied throughout the paper.

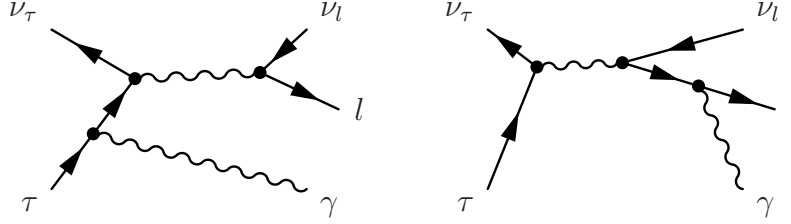


FIG. 1: Feynman diagram of the radiative leptonic decay of the τ lepton.

TABLE I: Michel parameters of the τ lepton

Name	SM value	Spin correlation	Experimental result [†] [7]	Comments and Ref.
η	0	no	0.013 ± 0.020	[8]
ρ	3/4	no	0.745 ± 0.008	[9]
$\xi\delta$	3/4	yes	0.746 ± 0.021	[9]
ξ	1	yes	0.995 ± 0.007	measured in hadronic decays [8]
$\bar{\eta}$	0	no	not measured	from radiative decay (RD)
$\xi\kappa$	0	yes	not measured	from RD
η''	0	no	not measured	from RD, suppressed by m_l^2/m_τ^2
ξ'	1	yes	-	induced from $\xi' = -\xi - 4\xi\kappa + 8\xi\delta/3$.

[†] Experimental results represent average values obtained by PDG [7]. The most precise results are referenced here.

$$\eta'' = \Re \{ 24g_{RL}^V(g_{LR}^{S*} + 6g_{LR}^{T*}) + 24g_{LR}^V(g_{RL}^{S*} + 6g_{RL}^{T*}) - 8(g_{RR}^Vg_{LL}^{S*} + g_{LL}^Vg_{RR}^{S*}) \}, \quad (7)$$

$$\xi\kappa = |g_{RL}^V|^2 - |g_{LR}^V|^2 + \frac{1}{8} \left(|g_{RL}^S + 2g_{RL}^T|^2 - |g_{LR}^S + 2g_{LR}^T|^2 \right) + 2 \left(|g_{RL}^T|^2 - |g_{LR}^T|^2 \right). \quad (8)$$

Both $\bar{\eta}$ and η'' appear as spin-independent terms in the differential decay width. Since all terms in Eq. 6 are strictly non-negative, the upper limit on $\bar{\eta}$ provides a constraint on each coupling constant. The effect of the nonzero value of η'' is suppressed by a factor of $m_l^2/m_\tau^2 \sim 10^{-7}$ for an electron daughter and $\sim 0.4\%$ for a muon daughter and so proves to be difficult to measure with the available statistics of the Belle experiment. In this study, we use the SM value $\eta'' = 0$.

To measure $\xi\kappa$, which appears in the spin-dependent part of the differential decay width, we must determine the spin direction of the τ . This spin dependence is extracted using the spin-spin correlation with the partner τ in the event. According to Ref. [5], $\xi\kappa$ is related to another Michel-like parameter $\xi' = -\xi - 4\xi\kappa + 8\xi\delta/3$. Because the normalized probability that the τ^- decays into the right-handed charged daughter lepton Q_R^τ is given by $Q_R^\tau = (1 - \xi')/2$ [6], the measurement of $\xi\kappa$ provides a further constraint on the $V - A$ structure of the weak current. The information on these parameters is summarized in Table I.

Using the statistically abundant data set of ordinary leptonic decays, previous measurements [8, 9] had determined the Michel parameters η , ρ , δ and ξ to an accuracy of a few percent and in agreement with the SM prediction. Taking into account this measured agreement, the smaller data set of the radiative decay and its limited sensitivity, we focus in this analysis only on the extraction of $\bar{\eta}$ and $\xi\kappa$ by fixing η , ρ , δ and ξ to the SM values. This represents the first measurement of the $\bar{\eta}$ and $\xi\kappa$ parameters of the τ lepton.

METHOD

Hereafter, we use an italic character to represent the four-vector p while its time and spatial components are denoted by capital letters as $p = (E, \mathbf{P})$. The magnitude of \mathbf{P} is denoted as P .

The differential decay width for the radiative leptonic decay of τ^- with a definite spin direction \mathbf{S}_{τ^-} is given by

$$\frac{d\Gamma(\tau^- \rightarrow l^- \nu \bar{\nu} \gamma)}{dE_l^* d\Omega_l^* dE_\gamma^* d\Omega_\gamma^*} = (A_0^- + \bar{\eta} A_1^-) + (\mathbf{B}_0^- + \xi \kappa \mathbf{B}_1^-) \cdot \mathbf{S}_{\tau^-}, \quad (9)$$

where A_i^- and \mathbf{B}_i^- are known functions of the kinematics of the decay products with indices $i = 0, 1$ (i simply denotes the name of function), Ω_a stands for a set of $\{\cos\theta_a, \phi_a\}$ for a particle type a and the asterisk means that the variable is defined in the τ rest frame. The detailed formula is given in Appendix A. Equation 9 shows that $\xi\kappa$ appears in the *spin-dependent* part of the decay width. This product can be measured by utilizing the well-known spin-spin correlation of the τ pair in the $e^-e^+ \rightarrow \tau^+\tau^-$ reaction:

$$\frac{d\sigma(e^-e^+ \rightarrow \tau^-(\mathbf{S}^-)\tau^+(\mathbf{S}^+))}{d\Omega_\tau} = \frac{\alpha^2 \beta_\tau}{64E_\tau^2} (D_0 + \sum_{i,j} D_{ij} S_i^- S_j^+), \quad (10)$$

where α is the fine structure constant, β_τ and E_τ are the velocity and energy of the τ , respectively, D_0 is a form factor for the spin-independent part of the reaction and D_{ij} ($i, j = 0, 1, 2$) is a tensor describing the spin-spin correlation [10]:

$$D_0 = 1 + \cos^2 \theta + \frac{1}{\gamma_\tau^2} \sin^2 \theta, \quad (11)$$

$$D_{ij} = \begin{pmatrix} (1 + \frac{1}{\gamma_\tau^2}) \sin^2 \theta & 0 & \frac{1}{\gamma_\tau} \sin 2\theta \\ 0 & -\beta_\tau^2 \sin^2 \theta & 0 \\ \frac{1}{\gamma_\tau} \sin 2\theta & 0 & 1 + \cos^2 \theta - \frac{1}{\gamma_\tau^2} \sin^2 \theta \end{pmatrix}; \quad (12)$$

here, θ is the polar angle of the τ^- and γ_τ is its gamma factor $1/\sqrt{1 - \beta_\tau^2}$.

The spin information on the partner τ^+ is extracted using the two-body decay $\tau^+ \rightarrow \rho^+ \bar{\nu} \rightarrow \pi^+ \pi^0 \bar{\nu}$ whose differential decay width is

$$\frac{d\Gamma(\tau^+ \rightarrow \pi^+ \pi^0 \bar{\nu})}{d\Omega_\rho^* dm^2 d\tilde{\Omega}_\pi} = A^+ + \mathbf{B}^+ \cdot \mathbf{S}_{\tau^+}; \quad (13)$$

A^+ and \mathbf{B}^+ are the form factors for the spin-independent and spin-dependent parts, respectively, while the tilde indicates the variables defined in the ρ rest frame and m is an invariant mass of the two-body system of pions which is defined as $m^2 = (p_\pi + p_{\pi^0})^2$. The formulae of A^+ and \mathbf{B}^+ are given in Appendix B. Thus, the total differential cross section of $e^+e^- \rightarrow \tau^-\tau^+ \rightarrow (l^-\nu\bar{\nu}\gamma)(\pi^+\pi^0\bar{\nu})$ (or, briefly, $(l^-\gamma, \pi^+\pi^0)$) can be written as:

$$\frac{d\sigma(l^-\gamma, \pi^+\pi^0)}{dE_l^* d\Omega_l^* dE_\gamma^* d\Omega_\gamma^* d\Omega_\rho^* dm^2 d\tilde{\Omega}_\pi d\Omega_\tau} \propto \frac{\beta_\tau}{E_\tau^2} \left[D_0 (A_0^- + A_1^- \cdot \bar{\eta}) A^+ + \sum_{i,j} D_{ij} (\mathbf{B}_0^- + \mathbf{B}_1^- \cdot \xi \kappa)_i \cdot \mathbf{B}_j^+ \right]. \quad (14)$$

To extract the visible differential cross section, we transform the differential variables into ones defined in the center-of-mass system (CMS) using the Jacobian J ($dE_l^* d\Omega_l^* dE_\gamma^* d\Omega_\gamma^* d\Omega_\rho^* d\Omega_\tau \rightarrow$

$d\Phi dP_l d\Omega_l dP_\gamma d\Omega_\gamma dP_\rho d\Omega_\rho$):

$$J = J_1 J_2 J_3, \quad (15)$$

$$J_1 = \left| \frac{\partial(E_l^*, \Omega_l^*)}{\partial(P_l, \Omega_l)} \right| = \frac{P_l^2}{E_l P_l^*}, \quad (16)$$

$$J_2 = \left| \frac{\partial(E_\gamma^*, \Omega_\gamma^*)}{\partial(P_\gamma, \Omega_\gamma)} \right| = \frac{E_\gamma}{E_\gamma^*}, \quad (17)$$

$$J_3 = \left| \frac{\partial(\Omega_\rho^*, \Omega_\tau)}{\partial(P_\rho, \Omega_\rho, \Phi)} \right| = \frac{m_\tau P_\rho}{E_\rho P_\rho^* P_\tau}, \quad (18)$$

where the parameter Φ denotes the angle along the arc illustrated in Fig. 2. On the assumption that the neutrino is massless and the invariant mass of the neutrino pair is greater than or equal to zero, we obtain

$$0 = p_\nu^2 = (p_\tau - p_\rho)^2 = m_\tau^2 + m^2 - 2E_\tau E_\rho + 2P_\tau P_\rho \cos\theta_{\tau\rho}, \quad (19)$$

$$0 \leq p_{\nu\bar{\nu}}^2 = (p_\tau - p_{l\gamma})^2 = m_\tau^2 + m_{l\gamma}^2 - 2E_\tau E_{l\gamma} + 2P_\tau P_{l\gamma} \cos\theta_{\tau(l\gamma)}. \quad (20)$$

$$\cos\theta_{\tau\rho} = \frac{2E_\tau E_\rho - m_\tau^2 - m^2}{2P_\tau P_\rho}, \quad (21)$$

$$\cos\theta_{\tau(l\gamma)} \geq \frac{2E_\tau E_{l\gamma} - m_\tau^2 - m_{l\gamma}^2}{2P_\tau P_{l\gamma}}. \quad (22)$$

In the back-to-back topology of the $\tau^+\tau^-$ pair, these two conditions constrain the τ^+ direction to the arc, with the angle Φ defined along this arc. The visible differential cross section is, therefore, obtained by integration over Φ :

$$\frac{d\sigma(l^-\gamma, \pi^+\pi^0)}{dP_l d\Omega_l dP_\gamma d\Omega_\gamma dP_\rho d\Omega_\rho dm^2 d\tilde{\Omega}_\pi} = \int_{\Phi_1}^{\Phi_2} d\Phi \frac{d\sigma(l^-\gamma, \pi^+\pi^0)}{d\Phi dP_l d\Omega_l dP_\gamma d\Omega_\gamma dP_\rho d\Omega_\rho dm^2 d\tilde{\Omega}_\pi} \quad (23)$$

$$= \int_{\Phi_1}^{\Phi_2} d\Phi \frac{d\sigma(l^-\gamma, \pi^+\pi^0)}{dE_l^* d\Omega_l^* dE_\gamma^* d\Omega_\gamma^* dm^2 d\tilde{\Omega}_\pi d\Omega_\tau} J \quad (24)$$

$$\equiv S(\mathbf{x}), \quad (25)$$

where $S(\mathbf{x})$ is proportional to the probability density function (PDF) of the signal and \mathbf{x} denotes the set of twelve measured variables: $\mathbf{x} = \{P_l, \Omega_l, P_\gamma, \Omega_\gamma, P_\rho, \Omega_\rho, m^2, \tilde{\Omega}_\pi\}$.

In general, the normalization of the PDF depends on the Michel parameters. Since $S(\mathbf{x})$ is a linear combination of the Michel parameters $S(\mathbf{x}) = A_0(\mathbf{x}) + A_1(\mathbf{x})\bar{\eta} + A_2(\mathbf{x})\xi\kappa$, the PDF is normalized according to

$$\frac{S(\mathbf{x})}{\int d\mathbf{x} S(\mathbf{x})} = \frac{A_0(\mathbf{x}) + A_1(\mathbf{x})\bar{\eta} + A_2(\mathbf{x})\xi\kappa}{\int d\mathbf{x} (A_0(\mathbf{x}) + A_1(\mathbf{x})\bar{\eta} + A_2(\mathbf{x})\xi\kappa)} \equiv \frac{A_0(\mathbf{x}) + A_1(\mathbf{x})\bar{\eta} + A_2(\mathbf{x})\xi\kappa}{N_0 + N_1\bar{\eta} + N_2\xi\kappa}, \quad (26)$$

where N_i ($i = 0, 1, 2$) is a normalization coefficient defined by $N_i = \int d\mathbf{x} A_i(\mathbf{x})$. This integration is performed using the Monte Carlo (MC) method. Since MC events are distributed according to the SM distribution ($\bar{\eta} = \xi\kappa = 0$), the denominator of Eq. 26 is

$$\int d\mathbf{x} (A_0(\mathbf{x}) + A_1(\mathbf{x})\bar{\eta} + A_2(\mathbf{x})\xi\kappa) = N_0 \int d\mathbf{x} \left(\frac{A_0(\mathbf{x})}{N_0} \right) \cdot \frac{A_0(\mathbf{x}) + A_1(\mathbf{x})\bar{\eta} + A_2(\mathbf{x})\xi\kappa}{A_0(\mathbf{x})} \quad (27)$$

$$= \frac{N_0}{N_{\text{gen}}} \sum_{i:\text{gen}} \frac{A_0(\mathbf{x}^i) + A_1(\mathbf{x}^i)\bar{\eta} + A_2(\mathbf{x}^i)\xi\kappa}{A_0(\mathbf{x}^i)} \quad (28)$$

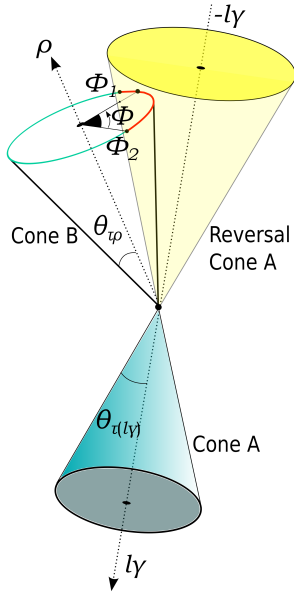


FIG. 2: Kinematics of $\tau^+\tau^- \rightarrow (\rho^+\bar{\nu})(l^-\nu\bar{\nu}\gamma)$ decay. Cones A and B are the surfaces that satisfy the conditions $(p_{\tau^-} - p_{l^-\gamma})^2 = 0$ and $(p_{\tau^+} - p_{\rho^+})^2 = 0$ in the CMS frame. The direction of τ^+ is constrained to lie on an arc defined by the intersection of the reversal (*i.e.*, mirror) cone A and cone B. The arc (shown in red) is parametrized by an angle $\Phi \in [\Phi_1, \Phi_2]$.

$$= N_0 \left[1 + \left\langle \frac{A_1}{A_0} \right\rangle \bar{\eta} + \left\langle \frac{A_2}{A_0} \right\rangle \xi \kappa \right], \quad (29)$$

where \mathbf{x}^i represents a set of variables for i^{th} generated event out of total N_{gen} events and the bracket $\langle \rangle$ means an average with respect to the SM distribution. We refer to N_0 and $\langle A_i/A_0 \rangle$ ($i = 1, 2$) as absolute and relative normalizations, respectively.

KEKB ACCELERATOR

The KEKB accelerator, located at KEK in Tsukuba, Ibaraki, Japan, is an energy-asymmetric e^+e^- collider with beam energies of 3.5 GeV and 8.0 GeV for e^+ and e^- , respectively. Most of the data taking was in operation at the CMS energy of 10.58 GeV, a mass of the $\Upsilon(4S)$, where a huge number of $\tau^+\tau^-$ as well as $B\bar{B}$ pairs were produced. The KEKB was operated from 1999 to 2010 and accumulated 1 ab^{-1} of e^+e^- collision data with Belle detector. The achieved instantaneous luminosity of $2.11 \times 10^{34} \text{ cm}^{-2}/\text{s}$ is the world-largest record. For this reason, the KEKB is often called *B-factory* but it is worth considering also as *tau-factory*, where $O(10^9)$ events of τ pair have been produced. The large number of the τ leptons and the dedicated detector provide a beautiful laboratory for the test of the nature of the rare decay $\tau^- \rightarrow l^-\nu\bar{\nu}\gamma$. The KEKB is described in detail in Refs. [11].

BELLE DETECTOR

The Belle detector is a large-solid-angle magnetic spectrometer that consists of a silicon vertex detector (SVD), a 50-layer central drift chamber (CDC), an array of aerogel threshold Cherenkov counters (ACC), a barrel-like arrangement of time-of-flight scintillation counters (TOF), and an electromagnetic calorimeter comprised of CsI(Tl) crystals (ECL) located inside a superconducting solenoid coil that provides a 1.5 T magnetic field. An iron flux return located outside of the coil is instrumented to detect K_L^0 mesons and to identify muons (KLM). The

detector is described in detail elsewhere [12].

EVENT SELECTION

The selection proceeds in two stages. At the preselection, $\tau^+\tau^-$ candidates are selected efficiently while suppressing the beam background and other physics processes like Bhabha scattering, two-photon interaction and $\mu^+\mu^-$ pair production. The preselected events are then required to satisfy final selection criteria to enhance the purity of the radiative events.

Preselection

- There must be exactly two oppositely charged tracks in the event. The impact parameters of these tracks relative to the interaction point are required to be within ± 2.5 cm along the beam axis and ± 0.5 cm in the transverse plane. The transverse momentum of two tracks must exceed 0.1 GeV/ c and that of one track must exceed 0.5 GeV/ c .
- Total energy deposition of ECL in the laboratory frame must be lower than 9 GeV.
- The opening angle ψ of the two tracks must satisfy $20^\circ < \psi < 175^\circ$.
- The number of photons whose energy exceeds 80 MeV in the CMS frame must be fewer than five.
- For the four-vector of missing momentum defined by $p_{\text{miss}} = p_{\text{beam}} - p_{\text{obs}}$, the missing mass M_{miss} defined as $M_{\text{miss}}^2 = p_{\text{miss}}^2$ must lie in the range $1 \text{ GeV}/c^2 \leq M_{\text{miss}} \leq 7 \text{ GeV}/c^2$, where p_{beam} and p_{obs} are the four-momentum of the beam and all detected particles, respectively.
- The missing-momentum's polar angle must satisfy $30^\circ \leq \theta_{\text{miss}} \leq 150^\circ$.

Final selection

The candidates of the daughter particles of $\tau^+\tau^- \rightarrow (\pi^+\pi^0\nu)(l^-\nu\bar{\nu}\gamma)$, *i.e.*, the lepton, photon, and charged and neutral pions, are assigned in each of the preselected events.

- The lepton candidate is selected using likelihood-ratio values. The electron selection uses $P_e = L_e/(L_e + L_x) > 0.9$, where L_e and L_x are the track's likelihood values for the electron and non-electron hypotheses, respectively. These values are determined using specific ionization (dE/dx) in the CDC, the ratio of ECL energy and CDC momentum E/P , the transverse shape of the cluster in the ECL, the matching of the track with the ECL cluster and the light yield in the ACC [13]. The muon selection uses the likelihood ratio $P_\mu = L_\mu/(L_\mu + L_\pi + L_K) > 0.9$, where the likelihood values are determined by the measured vs expected range for the μ hypothesis and transverse scattering of the track in the KLM [14]. The reductions of the signal efficiencies with lepton selections are approximately 2% and 3% for the electron and muon, respectively. The pion candidates are distinguished from kaons using $P_\pi = L_\pi/(L_\pi + L_K) > 0.4$, where the likelihood values are determined by the ACC response, the timing information from the TOF and dE/dx in the CDC. The reduction of the efficiency with pion selection is approximately 5%.
- The π^0 candidate is formed from two photon candidates, where each photon satisfies $E_\gamma > 80$ MeV, with an invariant mass of $115 \text{ MeV}/c^2 < M_{\gamma\gamma} < 150 \text{ MeV}/c^2$. Figure 3 shows the distribution of the invariant mass of the π^0 candidates. The reduction of the signal efficiency is approximately 24%.

- The ρ candidate is formed from a π and a π^0 candidate, with an invariant mass of $0.5 \text{ GeV}/c^2 < M_{\pi\pi^0} < 1.5 \text{ GeV}/c^2$. Figure 4 shows the distribution of the invariant mass of the ρ candidates. The reduction of the signal efficiency is approximately 3%.
- The signal photon candidate's energy must exceed 80 MeV if within the ECL barrel ($31.4^\circ < \theta_\gamma < 131.5^\circ$) or 100 MeV if within the ECL endcaps ($12.0^\circ < \theta_\gamma < 31.4^\circ$ or $131.5^\circ < \theta_\gamma < 157.1^\circ$). As shown in Fig. 5, this photon must lie in a cone determined by the lepton-candidate direction that is defined by $\cos\theta_{e\gamma} > 0.9848$ and $\cos\theta_{\mu\gamma} > 0.9700$ for the electron and muon mode, respectively. The reductions of the signal efficiencies for the requirement on this photon direction are approximately 11% and 27% for electron and muon mode, respectively. Furthermore, if the photon candidate and either of the photons from the π^0 , which is a daughter of the ρ candidate, form an invariant mass of the π^0 ($115 \text{ MeV}/c^2 < M_{\gamma\gamma} < 150 \text{ MeV}/c^2$), the event is rejected. The additional selection reduces the signal efficiencies by 1%.
- The direction of the combined momentum of the lepton and photon in the CMS frame must not enter the hemisphere determined by the ρ candidate: event should satisfy $\theta_{(l\gamma)\rho} > 90^\circ$. This selection reduces the signal efficiency by 0.4%.
- There must be no additional photons in the aforementioned cone around the lepton candidate; the sum of the energy in the laboratory frame of all additional photons that are not associated with the π^0 or the signal photon (denoted as $E_{\text{extra}\gamma}^{\text{LAB}}$) should not exceed 0.2 GeV and 0.3 GeV for the electron and muon mode, respectively. The reductions of the signal efficiencies for the requirement on the $E_{\text{extra}\gamma}^{\text{LAB}}$ are approximately 14% and 6% for electron and muon mode, respectively.

These selection criteria are optimized using a MC method where $e^+e^- \rightarrow \tau^+\tau^-$ pair production and the successive decay of the τ are simulated by KKMC [15] and TAUOLA [16, 17] generators, respectively. The detector effects are simulated based on the GEANT3 package [18].

The selection criteria suppress background while retaining efficiency for signal events. A characteristic feature of the radiative decay is that the photon tends to be produced nearly collinear with the final-state lepton. Distributions of the photon energy E_γ and the angle between the lepton and photon $\theta_{l\gamma}$ for the selected events are shown in Figs. 6 and 7 for $\tau^- \rightarrow e^- \nu \bar{\nu} \gamma$ and $\tau^- \rightarrow \mu^- \nu \bar{\nu} \gamma$ candidates, respectively.

In the electron mode, the fraction of the signal decay in the selected sample is about 30% due to the large external bremsstrahlung rate in the non-radiative leptonic τ decay events. In the muon mode, the fraction of the signal decay is about 60%; here, the main background arises from ordinary leptonic decay ($\tau^- \rightarrow l^- \nu \bar{\nu}$) events where either an additional photon is reconstructed from a beam background in the ECL or a photon is emitted by the initial-state e^+e^- .

With the described selection criteria, the average efficiencies of signal events are evaluated by MC. The selection information is summarized in Table II.

ANALYSIS

Accounting for the event-selection criteria and the contamination from identified backgrounds, the total visible (properly normalized) PDF for the observable \mathbf{x} in each event is given by

$$P(\mathbf{x}) = (1 - \sum_i \lambda_i) \frac{S(\mathbf{x})\varepsilon(\mathbf{x})}{\int d\mathbf{x} S(\mathbf{x})\varepsilon(\mathbf{x})} + \sum_i \lambda_i \frac{B_i(\mathbf{x})\varepsilon(\mathbf{x})}{\int d\mathbf{x} B_i(\mathbf{x})\varepsilon(\mathbf{x})}, \quad (30)$$

where $S(\mathbf{x})$ is the signal distribution given by Eq. 14, $B_i(\mathbf{x})$ is the distribution of the i^{th} category of background (i runs 1, 2, 3 and 1, 2, \dots , 6 for electron and muon modes, respectively

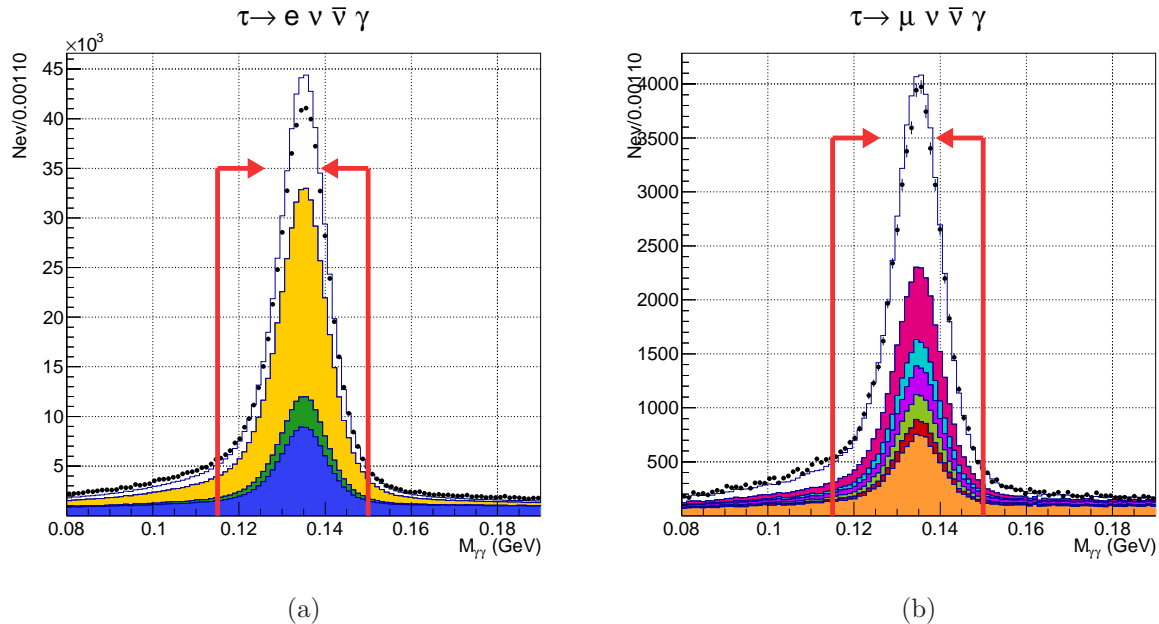


FIG. 3: Distribution of $M_{\gamma\gamma}$. Dots with error bars are experimental data and histograms are MC distributions. The MC histograms are scaled to that of experimental one based on the numbers just after the preselection. The red arrows indicate the selection window $115 \text{ MeV}/c^2 < M_{\gamma\gamma} < 150 \text{ MeV}/c^2$. The reduction of the efficiency is approximately 24% for both electron and muon modes.

(a) $\tau \rightarrow e\nu\bar{\nu}\gamma$ candidates: the open histogram corresponds to the signal, the yellow and green histograms represent ordinary leptonic decay plus bremsstrahlung and radiative leptonic decay plus bremsstrahlung, respectively, and the blue histogram represents other processes.

(b) $\tau \rightarrow \mu\nu\bar{\nu}\gamma$ candidates: the open histogram corresponds to signal, the magenta histogram represents ordinary leptonic decay plus beam background, the water-blue histogram represents ordinary leptonic decay plus ISR/FSR processes, the purple histogram represents three-pion events where $\tau^+ \rightarrow \pi^+\pi^0\pi^0\bar{\nu}$ is misreconstructed as a tagging $\tau^+ \rightarrow \pi^+\pi^0\bar{\nu}$ candidate, the green histogram represents ρ - ρ background where $\tau^- \rightarrow \pi^-\pi^0\nu$ is selected due to misidentification of pion as muon, the red histogram represents 3π - ρ events where $\tau^- \rightarrow \pi^-\pi^0\pi^0\nu$ is selected by misidentification similarly to the ρ - ρ case and the orange histogram represents other processes.

TABLE II: Summary of event selection

Item	$(e^-\nu\bar{\nu}\gamma)(\pi^+\pi^0\bar{\nu})$	$(e^+\nu\bar{\nu}\gamma)(\pi^-\pi^0\nu)$	$(\mu^-\nu\bar{\nu}\gamma)(\pi^+\pi^0\bar{\nu})$	$(\mu^+\nu\bar{\nu}\gamma)(\pi^-\pi^0\nu)$
N_{sel}	420005	412639	35984	36784
ε^\dagger (%)	4.45 ± 0.19	4.43 ± 0.19	3.42 ± 0.15	3.39 ± 0.15
Purity (%)	28.9		56.5	

[†] The signal is defined by the photon energy threshold in the τ -rest frame with $E_\gamma^* > 10 \text{ MeV}$.

and this index indicates each category filled with a color in Figs. 6 and 7), λ_i is the fraction of this background and $\varepsilon(\mathbf{x})$ is the selection efficiency of signal distribution. In general, the $\varepsilon(\mathbf{x})$ is not common between the signal and backgrounds, the difference, however, is included in the definition of $B_i(\mathbf{x})$. The PDFs of the major background modes are basically described using their theoretical formulae while other minor contributions are treated as one category

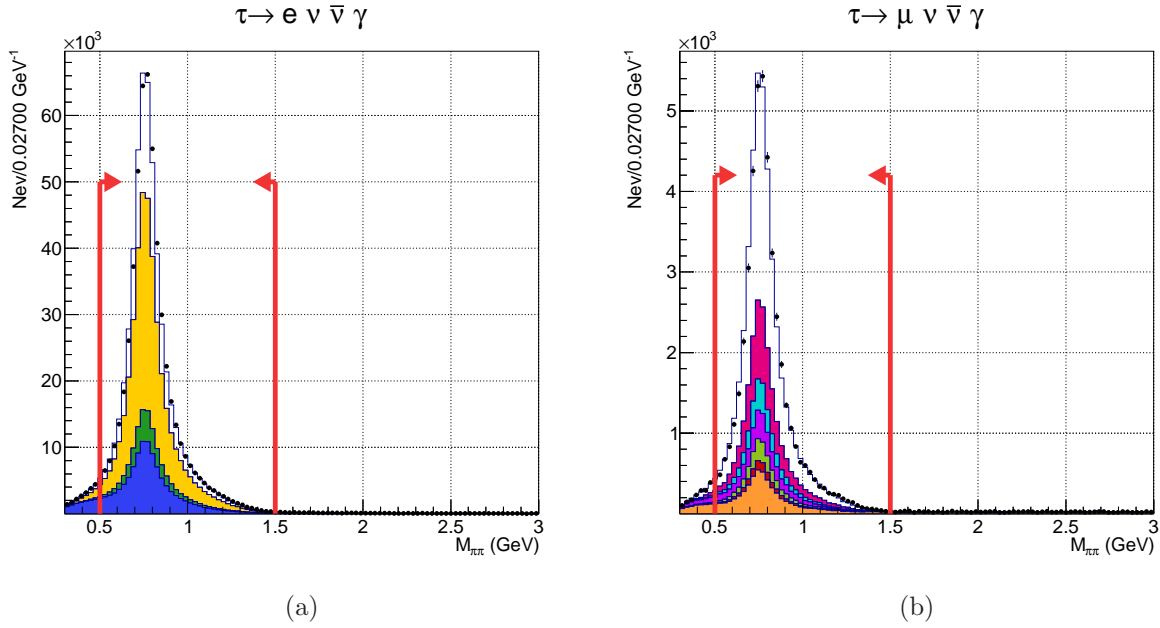


FIG. 4: Distribution of $M_{\pi\pi^0}$: (a) $\tau \rightarrow e\nu\bar{\nu}\gamma$ candidates and (b) $\tau \rightarrow \mu\nu\bar{\nu}\gamma$ candidates. Dots with error bars are experimental data and histograms are MC distributions. The color of each histogram is explained in Fig. 3. The red arrows indicate the selection window $0.5 \text{ GeV}/c^2 < M_{\pi\pi^0} < 1.5 \text{ MeV}/c^2$. The reduction of the efficiency is approximately 3% both for electron and muon modes.

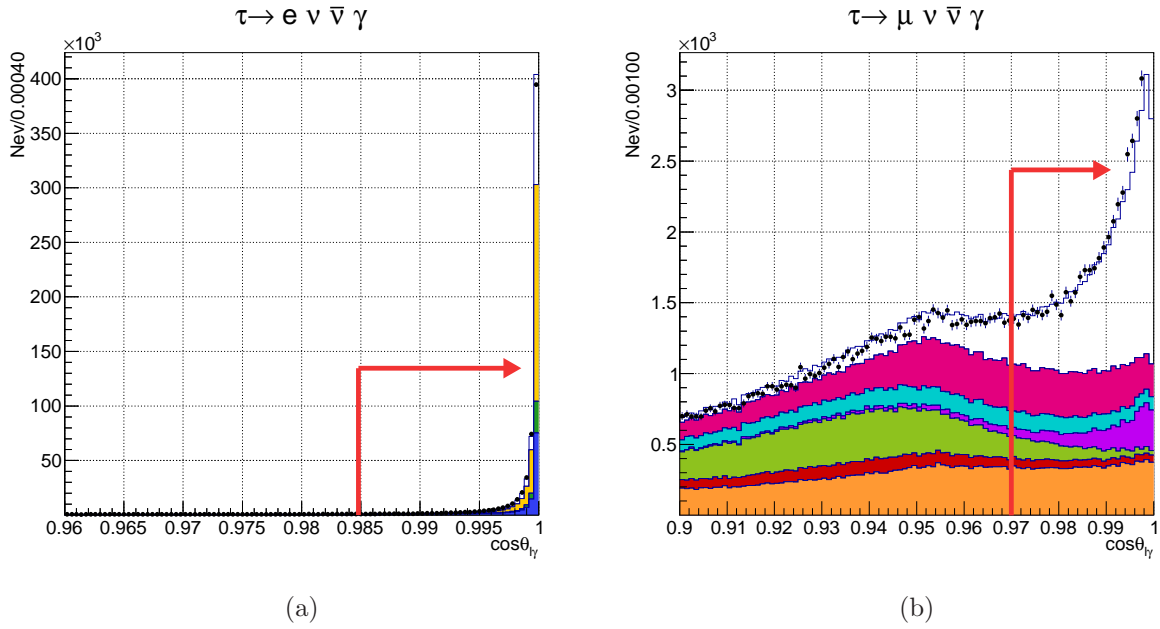


FIG. 5: Distribution of $\cos\theta_{l\gamma}$: (a) $\tau \rightarrow e\nu\bar{\nu}\gamma$ candidates and (b) $\tau \rightarrow \mu\nu\bar{\nu}\gamma$ candidates. Dots with error bars are experimental data and histograms are MC distributions. The color of each histogram is explained in Fig. 3. The red arrows indicate the selection condition $\cos\theta_{e\gamma} > 0.9848$ and $\cos\theta_{\mu\gamma} > 0.9700$ for the electron and muon mode, respectively. The reduction of the efficiency is approximately 11% and 27% for electron and muon modes.

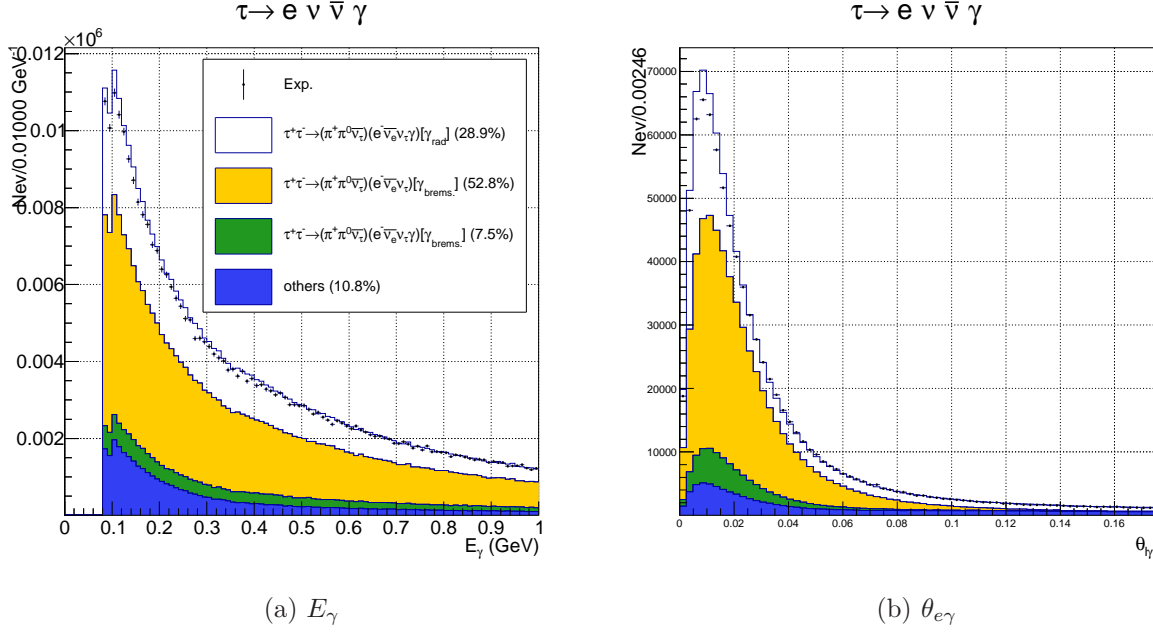


FIG. 6: Final distribution of (a) photon energy E_γ and (b) $\theta_{e\gamma}$ for the $\tau^+\tau^- \rightarrow (\pi^+\pi^0\bar{\nu})(e^-\nu\bar{\nu}\gamma)$ decay candidates. Dots with error bars are experimental data and histograms are MC distributions. The color of each histogram is explained in Fig. 3.

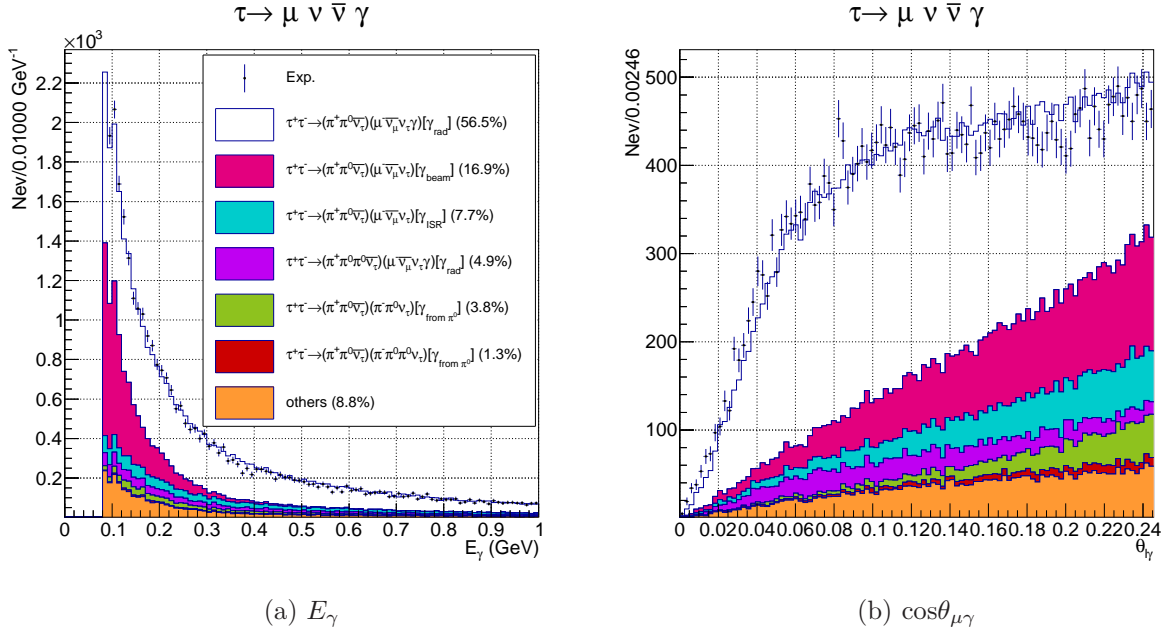


FIG. 7: Final distribution of (a) photon energy E_γ and (b) $\theta_{\mu\gamma}$ for the $\tau^+\tau^- \rightarrow (\pi^+\pi^0\bar{\nu})(\mu^-\nu\bar{\nu}\gamma)$ decay candidates. Dots with error bars are experimental data and histograms are MC distributions. The color of each histogram is explained in Fig. 3.

and described based on the MC simulation.

In the integration of the differential cross section over the Φ in Eq. 24, we randomly generate integration variables and calculate an average of the integrand. Moreover, an unfolding of the detector resolution is also performed in this integration, where the distortion of the momenta of the charged tracks and photon energies due to the finite accuracy of the detector is taken into account as a convolution with its resolution function determined from an MC simulation

of the detector. When the generated kinematic variables are outside allowed phase space of the signal distribution, we assign zero to the integrand rather than using its unphysical (negative) value. This means that we discard trials which have negative-mass neutrinos. If such discarded trials in the integration exceed 20% of the total number of iterations, we further reject the event. This happens for events which lie around the kinematical boundary of the signal phase space. The corresponding reduction of the efficiency is 2% and 3% for the electron and muon mode, respectively. This additional decrease of the efficiency is not reflected on the values of Table II.

From $P(\mathbf{x})$, the negative logarithmic likelihood function (NLL) is constructed and the best estimators of the Michel parameters, $\bar{\eta}$ and $\xi\kappa$, are obtained by minimizing the NLL. The efficiency $\varepsilon(\mathbf{x})$ is a common multiplier in Eq. 30 and does not depend on the Michel parameters. This is one of the essential features of the unbinned maximum likelihood method that we use. We validated our fitter and procedures using a MC sample generated according to the SM distribution. The fitted results are consistent with the SM predictions within 1σ statistical deviation of the experimental result.

Analysis of experimental data

The analysis of experimental data is performed in the same way as MC simulation. The difference between real data and MC simulation is represented by the measured correction factor $R(\mathbf{x}) = \varepsilon_{\text{ex}}(\mathbf{x})/\varepsilon_{\text{MC}}(\mathbf{x})$ that is close to unity; its extraction is described below. With this correction, Eq. 30 is modified to

$$P^{\text{ex}}(\mathbf{x}) = (1 - \sum_i \lambda_i) \cdot \frac{S(\mathbf{x})\varepsilon_{\text{MC}}(\mathbf{x})R(\mathbf{x})}{\int d\mathbf{x}S(\mathbf{x})\varepsilon_{\text{MC}}(\mathbf{x})R(\mathbf{x})} + \sum_i \lambda_i \frac{B_i(\mathbf{x})\varepsilon_{\text{MC}}(\mathbf{x})R(\mathbf{x})}{\int d\mathbf{x}B_i(\mathbf{x})\varepsilon_{\text{MC}}(\mathbf{x})R(\mathbf{x})}. \quad (31)$$

The presence of $R(\mathbf{x})$ in the numerator does not affect the NLL minimization, but its presence in the denominator does.

We evaluate $R(\mathbf{x})$ as the product of the measured corrections for the trigger, particle identifications and track reconstruction efficiencies:

$$R(\mathbf{x}) = R_{\text{trg}}R_l(P_l, \cos \theta_l)R_\gamma(P_\gamma, \cos \theta_\gamma)R_\pi(P_\pi, \cos \theta_\pi)R_{\pi^0}(P_{\pi^0}, \cos \theta_{\pi^0}), \quad (32)$$

$$R_l(P_l, \cos \theta_l) = R_{\text{rec.}}(P_l, \cos \theta_l)R_{\text{LID}}(P_l, \cos \theta_l), \quad (33)$$

$$R_\pi(P_\pi, \cos \theta_\pi) = R_{\text{rec.}}(P_\pi, \cos \theta_\pi)R_{\text{ID}}(P_\pi, \cos \theta_\pi). \quad (34)$$

The lepton identification efficiency correction is estimated using the two-photon processes $e^+e^- \rightarrow e^+e^-l^+l^-$ ($l = e$ or μ). Since the momentum of the lepton from the two-photon process ranges from 0 to approximately 4 GeV/ c in the laboratory frame, the efficiency correction factor can be evaluated for our signal process as a function of P_l and $\cos \theta_l$.

The track reconstruction efficiency correction is extracted from $\tau^+\tau^- \rightarrow (l^+\nu\bar{\nu})(\pi^-\pi^+\pi^-\nu)$ events. Here, we count the number of events N_4 (N_3) in which four (three) charged tracks are reconstructed. The three-charged-track event is required to have a negative net charge (π^+ is missing). Since the charged track reconstruction efficiency ε is included as, respectively, ε^4 and $\varepsilon^3(1 - \varepsilon)$ in N_4 and N_3 , the value of ε can be obtained by $\varepsilon = N_4/(N_4 + N_3)$.

The π^0 reconstruction efficiency correction is obtained by comparing the ratio of the number of selected events of $\tau^+\tau^- \rightarrow (\pi^+\pi^0\bar{\nu})(\pi^-\pi^0\nu)$ and $\tau^+\tau^- \rightarrow (\pi^+\pi^0\bar{\nu})(\pi^-\nu)$ between experiment and MC simulation. If we ignore one of the photon daughters from the π^0 , the γ reconstruction efficiency correction can be also extracted in the same manner.

The trigger efficiency correction has the largest impact among these factors. In particular, for the electron mode, because of the similar structure of our signal events and Bhabha events

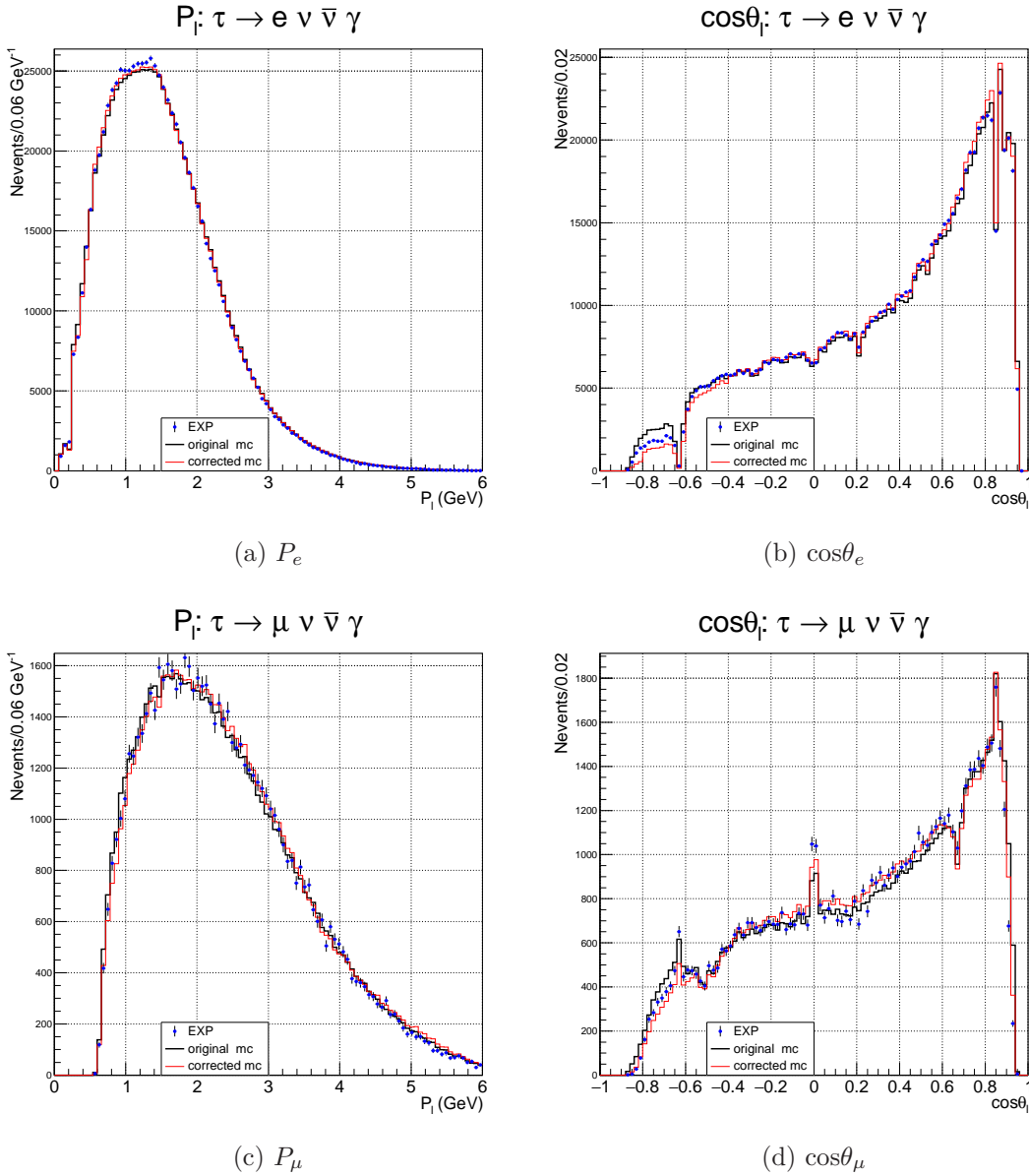


FIG. 8: Distribution of (a)(c) momentum and (b)(d) cosine of the lepton direction for (a)(b) $\tau \rightarrow e \nu \bar{\nu} \gamma$ and (c)(d) $\tau \rightarrow \mu \nu \bar{\nu} \gamma$ candidates. Blue points with error bars represent the experimental data. The black and red lines represent the distributions of the original and corrected MC, respectively.

(back-to-back topology of two-track events), many signal events are rejected by the Bhabha veto in the trigger. The veto of the trigger results in a spectral distortion and a large systematic uncertainty. The correction factor from trigger is tabulated using the charged and neutral triggers (denoted as Z and N), which provide completely independent signals. Since the trigger is fired when both signals are not inactive, its efficiency is given by $\varepsilon_{\text{trg}} = 1 - (1 - \varepsilon_Z)(1 - \varepsilon_N)$, where ε_Z and ε_N are, respectively, the efficiencies of the charged and neutral triggers. Here, each efficiency is extracted by a comparison of the numbers $N_{Z\&N}/N_N$ or $N_{Z\&N}/N_Z$. Thus R_{trg} is obtained as a ratio of ε_{trg} between the experiment and MC simulation. Through the R_{trg} , we incorporate this systematic bias and its uncertainty into our results.

Figure 8 shows the distribution of the momentum and the cosine of the polar angle of electron and muon events. In the figure, the effects of all corrections are seen mainly at $\cos\theta_e < -0.6$ and $\cos\theta_\mu < -0.6$.

TABLE III: List of systematic uncertainty contributions

Item	$\sigma_{\bar{\eta}}^e$	$\sigma_{\xi\kappa}^e$	$\sigma_{\bar{\eta}}^\mu$	$\sigma_{\xi\kappa}^\mu$
Relative normalizations	4.2	0.94	0.15	0.04
Absolute normalizations	1.0	0.01	0.03	0.001
Description of the background PDF	2.5	0.24	0.67	0.22
Input of branching ratio	3.8	0.05	0.25	0.01
Effect of cluster merge in ECL	2.2	0.46	0.02	0.06
Detector resolution	0.74	0.20	0.22	0.02
Correction factor R	1.9	0.14	0.04	0.04
Beam energy spread	negligible	negligible	negligible	negligible
Total	7.0	1.1	0.76	0.24

Evaluation of systematic uncertainties

In Table III, we summarize the contributions of various sources of systematic uncertainties. The dominant systematic source for the electron mode is the calculation of the relative normalizations. Due to the peculiarity of the signal PDF when $m_l \rightarrow 0$, the convergence of the factor is quite slow and results in a notable effect. The uncertainty of the relative normalization is evaluated using the central limit theorem. For a given number of MC events N , the errors of the relative normalizations $\langle A_i/A_0 \rangle$ ($i = 1, 2$) are evaluated by $\sigma^2 = \text{Var}(A_i/A_0)/N$, where $\text{Var}(X)$ represents the variance of a random variable X . The resulting systematic effect on the Michel parameter is estimated by varying the normalizations. The effect of the absolute normalization is estimated in the same way.

The largest systematic uncertainty for the muon mode is due to the limited precision of the description of the background PDF that appears in Eq. 31. As mentioned before, the set of minor sources is treated as one additional category that is based on MC distributions. This effective description can generally discard information about correlations in the phase space and thereby give significant bias. The residuals of the fitted Michel parameters from the SM prediction obtained by the fit to the MC distribution are taken as the corresponding systematic uncertainties.

Other notable uncertainties come from the limited knowledge of the measured branching ratios. In particular, the uncertainties of the branching ratio of the radiative decay $\tau^- \rightarrow l^- \nu \bar{\nu} \gamma$ dominate the contribution. The systematic effects of the cluster-merge algorithm in the ECL are evaluated as a function of the angle between the photon and lepton clusters at the ECL's front face ($\theta_{l\gamma}^{\text{ECL}}$). The limit $\theta_{l\gamma}^{\text{ECL}} \rightarrow 0$ represents the merger of the two clusters and the comparison of the distribution between experiment and MC gives us the corresponding bias. Detector resolutions of the photon energies and track momenta are evaluated by comparing the results obtained with and without the unfolding of the measured values. The error of the tabulated correction factor R is estimated by varying the central values based on the uncertainty in each bin. The effect of the beam-energy spread is estimated by varying the input of this value for the calculation of PDF with respect to run-dependent uncertainties.

RESULTS

Based on the PDF in Eq. 31, we construct the NLL function, minimize it and obtain the Michel parameters $\bar{\eta}$ and $\xi\kappa$. Since the sensitivity to $\bar{\eta}$ is suppressed by the factor of m_l/m_τ ,

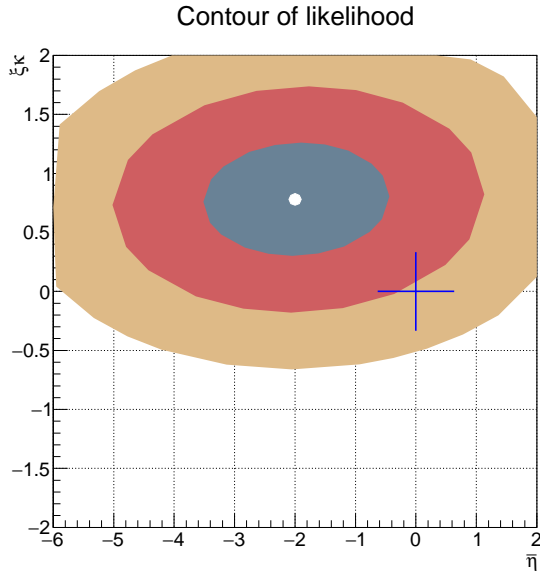


FIG. 9: Contour of the likelihood for $\tau \rightarrow \mu\nu\bar{\nu}\gamma$ events. The circles indicate 1σ , 2σ and 3σ statistical deviations from inner to outer side, respectively. The cross is the SM prediction.

we extract it from the muon mode only. Using 832644 and 72768 selected events, respectively, for $\tau^+\tau^- \rightarrow (\pi^+\pi^0\bar{\nu})(e^-\nu\bar{\nu}\gamma)$ and $\tau^+\tau^- \rightarrow (\pi^+\pi^0\bar{\nu})(\mu^-\nu\bar{\nu}\gamma)$ candidates, we obtain

$$(\xi\kappa)^{(e)} = -0.5 \pm 0.8 \pm 1.1, \quad (35)$$

$$\bar{\eta}^\mu = -2.0 \pm 1.5 \pm 0.8, \quad (36)$$

$$(\xi\kappa)^{(\mu)} = 0.8 \pm 0.5 \pm 0.2, \quad (37)$$

where the first error is statistical and the second is systematic. The results of $\xi\kappa$ are combined to give

$$\xi\kappa = 0.6 \pm 0.4 \pm 0.2. \quad (38)$$

Figure 9 shows the contour the likelihood for $\tau \rightarrow \mu\nu\bar{\nu}\gamma$ events. As the shape suggests, a correlation between $\bar{\eta}$ and $\xi\kappa$ is small. The magnitude of the correlation coefficient determined by the error matrix is approximately 7%.

SUMMARY

We present preliminary results of a measurement of the Michel parameters $\bar{\eta}$ and $\xi\kappa$ of the τ using 703 fb^{-1} of data collected with the Belle detector at the KEKB e^+e^- collider. These parameters are extracted from the radiative leptonic decay $\tau^- \rightarrow l^-\nu\bar{\nu}\gamma$ and the tagging ρ decay $\tau^+ \rightarrow \rho^+(\rightarrow \pi^+\pi^0)\bar{\nu}$ of the partner τ^+ to exploit the spin-spin correlation in $e^+e^- \rightarrow \tau^+\tau^-$. Due to the poor sensitivity to $\bar{\eta}$ in the electron mode, this parameter is extracted only from $\tau^- \rightarrow \mu^-\nu\bar{\nu}\gamma$ to give $\bar{\eta} = -2.0 \pm 1.5 \pm 0.8$. The product $\xi\kappa$ is measured using both decays $\tau^- \rightarrow l^-\nu\bar{\nu}\gamma$ ($l = e$ and μ) to be $\xi\kappa = 0.6 \pm 0.4 \pm 0.2$. The first error is statistical and the second is systematic. This is the first measurement of both parameters for the τ lepton. These values are consistent with the SM expectation within the errors.

ACKNOWLEDGMENTS

We thank the KEKB group for the excellent operation of the accelerator; the KEK cryogenics group for the efficient operation of the solenoid; and the KEK computer group, the National Institute of Informatics, and the PNNL/EMSL computing group for valuable computing and SINET4 network support. We acknowledge support from the Ministry of Education, Culture, Sports, Science, and Technology (MEXT) of Japan, the Japan Society for the Promotion of Science (JSPS), and the Tau-Lepton Physics Research Center of Nagoya University; the Australian Research Council; Austrian Science Fund under Grant No. P 22742-N16 and P 26794-N20; the National Natural Science Foundation of China under Contracts No. 10575109, No. 10775142, No. 10875115, No. 11175187, No. 11475187 and No. 11575017; the Chinese Academy of Science Center for Excellence in Particle Physics; the Ministry of Education, Youth and Sports of the Czech Republic under Contract No. LG14034; the Carl Zeiss Foundation, the Deutsche Forschungsgemeinschaft, the Excellence Cluster Universe, and the Volkswagen-Stiftung; the Department of Science and Technology of India; the Istituto Nazionale di Fisica Nucleare of Italy; the WCU program of the Ministry of Education, National Research Foundation (NRF) of Korea Grants No. 2011-0029457, No. 2012-0008143, No. 2012R1A1A2008330, No. 2013R1A1A3007772, No. 2014R1A2A2A01005286, No. 2014R1A2A2A01002734, No. 2015R1A2A2A01003280 , No. 2015H1A2A1033649; the Basic Research Lab program under NRF Grant No. KRF-2011-0020333, Center for Korean J-PARC Users, No. NRF-2013K1A3A7A06056592; the Brain Korea 21-Plus program and Radiation Science Research Institute; the Polish Ministry of Science and Higher Education and the National Science Center; the Ministry of Education and Science of the Russian Federation and the Russian Foundation for Basic Research, grant 15-02-05674; the Slovenian Research Agency; Ikerbasque, Basque Foundation for Science and the Euskal Herriko Unibertsitatea (UPV/EHU) under program UFI 11/55 (Spain); the Swiss National Science Foundation; the Ministry of Education and the Ministry of Science and Technology of Taiwan; and the U.S. Department of Energy and the National Science Foundation. This work is supported by a Grant-in-Aid from MEXT for Science Research in a Priority Area (“New Development of Flavor Physics”) and from JSPS for Creative Scientific Research (“Evolution of Tau-lepton Physics”).

-
- [1] W. Fetscher, H. J. Gerber and K. F. Johnson, Phys. Lett. **B173**, 102 (1986).
[2] W. Fetscher and H. J. Gerber, Adv. Ser. Direct. High Energy Phys. **14**, 657 (1995).
[3] C. Fronsdal and H. Uberall, Phys. Rev. **113**, 654 (1939).
[4] A. B. Arbuzov and T.V. Kopylova, arXiv:1605.06612[hepex] (2016).
[5] W. Fetscher and H. J. Gerber, ETH-IMP PR-93-1 (1993).
[6] A. Stahl and H. Voss, Z. Phys. **C74**, 73 (1997).
[7] K.A. Olive *et al.* (Particle Data Group), Chin. Phys. **C38**, 090001 (2014).
[8] A. Heister *et al.* (ALEPH Collaboration), Eur. Phys. J. **C22**, 217 (2001).
[9] J. P. Alexander *et al.* (CLEO Collaboration), Phys. Rev. **D56**, 5320 (1997).
[10] Y. S. Tsai, Phys. Rev. **D4**, 2821 (1971).
[11] S. Kurokawa and E. Kikutani, Nucl. Instrum. Methods Phys. Res. Sect. A **499**, 1 (2003), and other papers included in this Volume. T.Abe *et al.*, Prog. Theor. Exp. Phys. **2013**, 03A001 (2013) and references therein.
[12] A. Abashian *et al.* (Belle Collaboration), Nucl. Instrum. Methods Phys. Res. Sect. A **479**, 117 (2002); also see detector section in J.Brodzicka *et al.*, Prog. Theor. Exp. Phys. **2012**, 04D001 (2012).
[13] K. Hanagaki *et al.*, Nucl. Instrum. Meth. **A485**, 490 (2002).
[14] A. Abashian *et al.*, Nucl. Instrum. Meth. **A491**, 69 (2002).
[15] S. Jadach, B.F.L Ward, Z. Wąs, Comput. Phys. Commun. **130**, 260 (2000).
[16] Z. Wąs, Nucl. Phys. Proc. Suppl. **98**, 96 (2001).
[17] S. Jadach, Z. Wąs, Comput. Phys. Commun. **76**, 361 (1993).
[18] R. Brun, *et al.*, CERN-DD-78-2 (1978).
[19] S. Anderson *et al.* (CLEO Collaboration), Phys. Rev. **D61**, 112002 (2000).
[20] S. Jadach, J. H. Kühn and Z. Wąs, Comput. Phys. Commun. **64**, 275 (1991).

Appendix A: Differential decay width of $\tau \rightarrow l\nu\bar{\nu}\gamma$

The general differential cross section of $\tau \rightarrow l\nu\bar{\nu}\gamma$ decay is expressed as a sum of the two terms:

$$\frac{d\Gamma(\tau^\mp \rightarrow l^\mp \nu_\tau \bar{\nu}_l \gamma)}{dE_l^* d\Omega_l^* dE_\gamma^* d\Omega_\gamma^*} = A \mp \mathbf{B} \cdot \mathbf{S}_{\tau^\mp}, \quad (39)$$

where A and \mathbf{B} represent spin-independent and spin-dependent terms. These terms are functions of dimensionless kinematic parameters x, y and d defined as:

$$r = \frac{m_l}{m_\tau}, \quad (40)$$

$$x = \frac{2E_l^*}{m_\tau}, \quad (2r < x < 1 + r^2) \quad (41)$$

$$y = \frac{2E_\gamma^*}{m_\tau}, \quad (0 < y < 1 - r) \quad (42)$$

$$d = 1 - \beta_l^* \cos \theta_{l\gamma}^*, \quad (43)$$

$$y < \frac{2(1 + r^2 - x)}{2 - x + \cos \theta_{l\gamma}^* \sqrt{x^2 - 4r^2}}. \quad (44)$$

A and \mathbf{B} are parametrized by the Michel parameters $\rho, \eta, \xi, \xi\delta, \bar{\eta}, \eta''$ and $\xi\kappa$.

$$A(x, y, d) = \frac{4\alpha G_F^2 m_\tau^3}{3(4\pi)^6} \cdot \beta_l \sum_{i=0,1\dots 5} F_i r^i, \quad (45)$$

$$\mathbf{B}(x, y, d) = \frac{4\alpha G_F^2 m_\tau^3}{3(4\pi)^6} \cdot \beta_l \sum_{i=0,1\dots 5} (\beta_i^* G_i \mathbf{n}_i^* + H_i \mathbf{n}_\gamma^*) r^i, \quad (46)$$

where \mathbf{n}_i^* and \mathbf{n}_γ^* are normalized directions of lepton and photon in the τ rest frame, respectively. The F_i , G_i and H_i ($i = 0, 1 \dots 5$) are functions of x , y , d and r and their explicit formulae are given in the Appendix of Ref. [4].

Appendix B: Differential decay width of $\tau \rightarrow \rho\nu$

We use the CLEO model to define the differential decay width of $\tau^\pm \rightarrow \rho^\pm \nu$ decay. This is expressed as a sum of the spin-independent and spin-dependent parts [19, 20]:

$$\frac{d\Gamma(\tau^\pm \rightarrow \pi^\pm \pi^0 \nu)}{d\Omega_\rho^* dm^2 d\tilde{\Omega}_\pi} = A' \mp \mathbf{B}' \cdot \mathbf{S}_{\tau^\pm}, \quad (47)$$

$$A' = \frac{G_F^2 |V_{ud}|^2}{(4\pi)^5} \cdot \left[2(E_\pi^* - E_{\pi^0}^*)(p_\nu \cdot q) - E_\nu^* q^2 \right] \cdot \text{BPS}, \quad (48)$$

$$\mathbf{B}' = \frac{G_F^2 |V_{ud}|^2}{(4\pi)^5} \cdot \left[\mathbf{P}_\pi^* \{ (q \cdot q) + 2(p_\nu \cdot q) \} + \mathbf{P}_{\pi^0}^* \{ (q \cdot q) - 2(p_\nu \cdot q) \} \right] \cdot \text{BPS}, \quad (49)$$

where V_{ud} is the corresponding element of the Cabibbo-Kobayashi-Maskawa matrix and q is a four-vector defined by $q = p_\pi - p_{\pi^0}$. The factor BPS stands for a square of a relativistic Breit-Wigner function and a Lorentz-invariant phase space and it is calculated from the following formulae.

$$\text{BPS} = |\text{BW}(m^2)|^2 \left(\frac{2P_\rho^*(m^2)}{m_\tau} \right) \left(\frac{2\tilde{P}_\pi(m^2)}{m_\rho} \right), \quad \text{BW}(m^2) = \frac{\text{BW}_\rho + \beta \text{BW}_{\rho'}}{1 + \beta}, \quad (50)$$

$$\text{BW}_\rho(m^2) = \frac{m_{\rho 0}^2}{m_{\rho 0}^2 - m^2 - im_{\rho 0} \Gamma_\rho(m^2)}, \quad \Gamma_\rho(m^2) = \Gamma_{\rho 0} \frac{m_{\rho 0}}{\sqrt{m^2}} \left(\frac{\tilde{P}_\pi(m^2)}{\tilde{P}_\pi(m_{\rho 0}^2)} \right)^3, \quad (51)$$

$$\text{BW}_{\rho'}(m^2) = \frac{m_{\rho' 0}^2}{m_{\rho' 0}^2 - m^2 - im_{\rho' 0} \Gamma_{\rho'}(m^2)}, \quad \Gamma_{\rho'}(m^2) = \Gamma_{\rho' 0} \frac{m_{\rho' 0}}{\sqrt{m^2}} \left(\frac{\tilde{P}_\pi(m^2)}{\tilde{P}_\pi(m_{\rho' 0}^2)} \right)^3, \quad (52)$$

$$\tilde{P}_\rho^*(m^2) = \frac{m_\tau^2 - m^2}{2m_\tau} \quad (53)$$

$$\tilde{P}_\pi(m^2) = \frac{\sqrt{[m^2 - (m_\pi - m_{\pi^0})^2][m^2 - (m_\pi + m_{\pi^0})^2]}}{2m}. \quad (54)$$

A factor BW_a ($a = \rho$ or ρ') represents the Breit-Wigner function associated with a ρ or a ρ' resonance mass shape and the parameter β specifies their relative coupling. $m_{\rho 0}$ and $m_{\rho' 0}$ are nominal masses of two resonance states and $\Gamma_{\rho 0}$ and $\Gamma_{\rho' 0}$ are their nominal total decay widths.